Cation Vacancies in $NiFe_2O_4$ During Heat Treatments at High Temperatures: Structural, Morphological and Magnetic Characterization

Harrison Salazar-Tamayo[a]* , Karen Edilma García Tellez[a], César Augusto Barrero Meneses[a]

[a]Grupo de Estado Sólido, Facultad de Ciencias Exactas y Naturales, Universidad de Antioquia (UdeA), Calle 70, No 52-21, Medellín, Colombia

Nickel ferrite ($NiFe_2O_4$) was synthesized by mixing stoichiometric amounts of α-Fe_2O_3 and NiO using mechanical milling and heat treatments at high temperatures. The physical characterization of the samples was carried out using X-ray diffraction, infrared and Raman spectroscopies, Mössbauer spectrometry, magnetization measurements, scanning electron microscopy and energy dispersive X-ray spectroscopy. We found that $NiFe_2O_4$ production increases from 81 to 100 wt. % with increasing temperature. Additionally, the lattice parameter and the saturation magnetization increase with increasing temperature. On the other hand, Mössbauer spectrometry showed that there is a decrease in the subspectral areas ratio for Fe^{3+} cations at tetrahedral (A) and octahedral [B] sites, A_A/A_B, with the increase of the temperature. In the SEM micrographs it was observed that the samples consisted of particles with irregular shapes and micrometric sizes. From IR spectra, the intensity of the 411 cm^{-1} band (vibrations at octahedral sites) increases relative to the intensity of the 599 cm^{-1} band (vibrations at tetrahedral sites) with increasing temperature. From the results obtained in the magnetization curves, it was possible to confirm the synthesis of $NiFe_2O_4$. As the heat treatment temperature increases, hysteresis loops with S-type geometric forms were obtained. All the results suggest that a defective spinel $NiFe_2O_4$ is formed at 1000 °C, and that as the temperature increases, the defects gradually disappear. Neither cation reordering phenomena nor possible evaporation of chemical elements were the dominant effects to account for the results. The results can be explained if it is assumed that [B]-sites cation vacancies are gradually filled with cations as the temperature of the heat treatment increases.

Keywords: *$NiFe_2O_4$, spinel structure, solid state reaction, cation vacancies.*

1. Introduction

Ferrite is the common name of the materials with general chemical formula MFe_2O_4, where M is a divalent metal cation. The magnetic and structural properties of the ferrites are an open research field in materials science due to the wide range of applicability in technology and industry. Nickel ferrite, $NiFe_2O_4$ (M = Ni), is a material that has awakened great interest in the scientific community due to the good electromagnetic behavior and its applications in the storage of information. This material can be used to fabricate pieces of great strength and hardness. It also has other applications such as inductors, antennas, gas sensors, devices for the handling of microwaves, catalytic supports, spin filtering barriers in magnetic tunnel junctions, magnetic carrier for drug delivery, remover of Fe(II) from aqueous solutions, among others[1-5].

$NiFe_2O_4$ has been synthesized by several methods including sol-gel [6-7], coprecipitation [8], mechanical milling [9-10], combustion[11-12], thin films[3,13], solid state reaction[14-15], among others. Physical properties such as particle size, magnetic behavior, crystal structure, cation distributions, coercivity,

Néel temperatures, spin configurations, saturation magnetization, among others; may vary depending on the synthesis procedure. Solid-state reaction is a method of synthesis of polycrystalline materials that consists of the direct chemical reaction between solid materials (powders) at high temperatures. Among the advantages presented by this method, we find the low cost of reactants, the simplicity of the heat treatments and the purity of chemical reactions that allow avoiding external waste elements or contaminations.

On the other hand, we have noticed that in most of reported works for the $NiFe_2O_4$ ferrite, the authors concentrate their research in studying the physical properties of $NiFe_2O_4$ as final material. However, there are few studies reporting in detail the changes of the physical properties of this material during the synthesis process. For this reason, the present work can allow us to monitor the process of formation of the spinel structure and to have better comprehension of the physical-property changes of $NiFe_2O_4$ with the temperature of synthesis. Therefore, the main purpose of this work is to synthesize $NiFe_2O_4$ using the solid-state reaction method and to carefully analyze the variation of the structural, vibrational and magnetic properties with the temperature of the heat treatments.

*e-mail: harrison.salazar@udea.edu.co

2. Materials and Methods

Nickel ferrite ($NiFe_2O_4$) was synthesized by mixing stoichiometric amounts of hematite (α-Fe_2O_3) and nickel oxide (NiO). The crystalline powders were subjected to low-energy mechanical milling with the purpose to produce homogeneous mixtures of reactants. It is important to emphasize that during the milling process we want neither to induce chemical transformations nor to synthesize the spinel phase. The mechanical milling was performed at room temperature and atmospheric pressure in a Fritsch Pulverisette 5 planetary ball mill. Agate jars (250 mL) and agate balls (12 mm diameter) were used in the process. The angular velocity was 100 rpm, the ratio of the mass of the balls to the mass of the powder was of 30:1 and the milling time was 2 h. Subsequently, the powders were submitted to heat treatments at 1000, 1100 and 1200 °C for 12 h. The heating and cooling ramps were of 2 °C/min and 10 °C/min, respectively.

The physical characterization of the samples was carried out using X-ray diffraction, infrared and Raman spectroscopies, Mössbauer spectrometry, magnetization measurements, scanning electron microscopy and energy dispersive X-ray spectroscopy. The XRD patterns were obtained in a Panalytical diffractometer X'Pert PRO MPD using a Cu-Kα X-ray source. The measurements were performed in 2θ range of 10°-75° using steps of 0.04° and time per step of 23 s. The Rietveld analysis of the XRD patterns was carried out using the MAUD program, which allowed us to determine lattice parameters and relative abundances of the crystalline phases. To initiate the analysis, CIF files corresponding to the NiO (1010093 COD), α-Fe_2O_3 (9000139 COD) and $NiFe_2O_4$ (76179 ICSD) crystallographic phases were used as input data. In each crystalline phase, lattice parameters, average crystallite sizes, microstrains and relative abundances were refined. Arbitrary textures and isotropic crystallite sizes were assumed in the analysis. Regarding the instrumental parameters, the scale factor, sample displacement and background were refined.

The room temperature Mössbauer spectra were collected in the standard transmission geometry using a ^{57}Co/Rh radioactive source. The adjustment of the Mössbauer spectra was performed using lorentzian Mössbauer lines as implemented in the RECOIL program. The Mössbauer spectrum of a thin foil of α-Fe collected at room temperature was used for calibration purposes. Fourier transformed infrared spectroscopy was performed in a Shimadzu IRAffinity-1 spectrometer. The IR spectra were obtained in the wave number range 400-1500 cm^{-1} and in transmittance mode. The Raman spectra were obtained using a Horiba Jobin Yvon LabRAM HR spectrometer. An Olympus BX41 optical microscope with 50x objective and a He-Ne laser were used in the process. The SEM micrographs were obtained using a JEOL JSM-6490LV scanning electron microscope with magnifications of 5000x and 10000x. The EDS spectra were obtained using the Oxford Instruments INCA PentaFETx3 spectrometer coupled to the SEM instrument.

The magnetic behavior of the samples was studied using a Physical Property Measurement System at room temperature.

3. Results

Figure 1 shows the XRD patterns of the initial mixture of reactants and of the samples submitted to heat treatments. The first XRD pattern (Fig. 1(a)) corresponds to the sample without treatment heat. All peaks were identified with Miller indices corresponding to crystallographic planes of α-Fe_2O_3 and NiO. Figure 1(b) shows the XRD pattern of the sample submitted to heat treatment at 1000 °C. The (110), (006), (116), (122), (214), (300), (208) and (1010) diffraction peaks of α-Fe_2O_3 were not observed in the XRD pattern, while the remaining peaks of this phase experienced a drastic decrease in intensity. The (220) diffraction peak of NiO was not observed in the XRD pattern, while the (111) and (200) peaks of the same phase have decreased considerably in intensity and greatly overlap with the (222) and (400) peaks of $NiFe_2O_4$, respectively. In the same XRD pattern, we can notice the presence of the (111), (220), (311), (400), (422), (511), (440), (620) and (533) diffraction peaks related to $NiFe_2O_4$. Some of these peaks overlap with diffraction peaks of the reactants, however, it is observed a drastic increase in intensity (almost the double) of the peaks of $NiFe_2O_4$ in comparison to the peaks of the reactants. Considering the previous results, the sample submitted to heat treatment at 1000 °C consists of a mixture of α-Fe_2O_3, NiO and $NiFe_2O_4$, where the ferrite is the dominant phase.
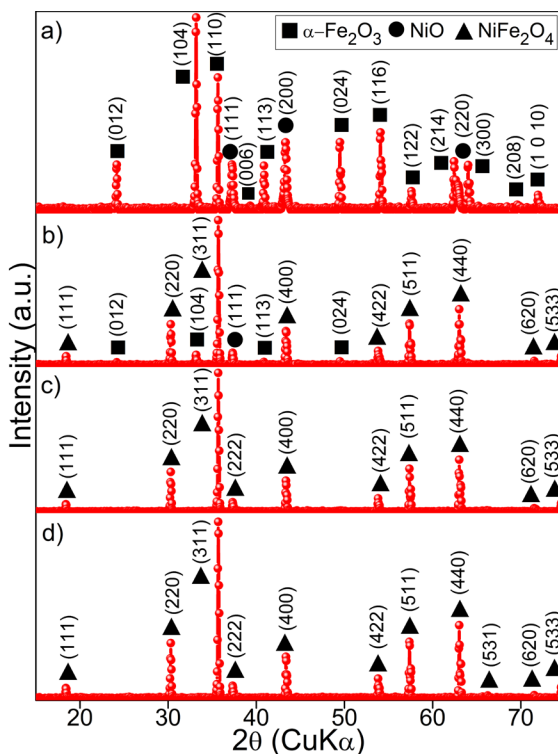

Figure 1. XRD patterns of (a) the initial mixture of reactants and of the samples submitted to heat treatments at (b) 1000 ºC, (c) 1100 ºC and (d) 1200 ºC.

Cation Vacancies in NiFe$_2$O$_4$ During Heat Treatments at High Temperatures: Structural, Morphological and Magnetic Characterization

3

Figure 1(c) shows the XRD pattern of the sample submitted to heat treatment at 1100 °C. The (012), (104), (113) and (024) diffraction peaks of α-Fe$_2$O$_3$ were not observed. The (111) and (200) peaks of NiO have almost disappeared and greatly overlap with the (222) and (400) peaks of NiFe$_2$O$_4$, which are the dominant ones. The remaining peaks related to the spinel phase increase in intensity. Taking into account the previous results, the sample submitted to heat treatment at 1100 °C corresponds to NiFe$_2$O$_4$, and the peaks related to reactants have almost disappeared. Finally, Figure 1(d) shows the XRD pattern of the sample submitted to heat treatment at 1200 °C. All diffraction peaks present in the XRD pattern correspond to NiFe$_2$O$_4$, which confirms the synthesis of the material.

Figure 2 shows the Rietveld refinement of the XRD patterns of the initial mixture of reactants and of the samples submitted to heat treatments. The quality of the Rietveld refinements was determined using a set of conventional statistical parameters. In general, the quality of the Rietveld refinement (goodness of fit),χ^2, can be determined using the statistical parameters R_{wp} (Weight Profile R-factor) and R_{exp} (Expected R-Factor), where R_{wp} compares the adjusted data with the experimental data and R_{exp} evaluates the quality of the experimental data. The previous parameters are related through the equation $\chi^2 = (R_{wp}/R_{exp})^2$. During the refinement process, χ^2 begins with large values when the fit model is poor and decreases as the fit data matches the experimental data. The refinement continues until convergence is reached with values close to 1, which indicates a correlation between the experimental data and the adjustment model used. Table 1 shows the values of the R_{wp}, R_{exp}, and χ^2 statistical parameters obtained in the Rietveld refinement of the XRD patterns.

The XRD pattern of the initial mixture of reactants (Fig. 2(a)) was adjusted using the NiO (1010093 COD) and α-Fe$_2$O$_3$ (9000139 COD) crystalline phases. The results of the Rietveld analysis for NiO give a lattice parameter of a = 4.178 Å and an abundance of 32 wt. %. For α-Fe$_2$O$_3$, lattice parameters of a = 5.030 Å and b = 13.740 Å, and an abundance of 68 wt. % were obtained. The abundances found for NiO and α-Fe$_2$O$_3$ coincide within an error of about 1 wt.% with the weight percentages found in the stoichiometric equations of the chemical reaction.
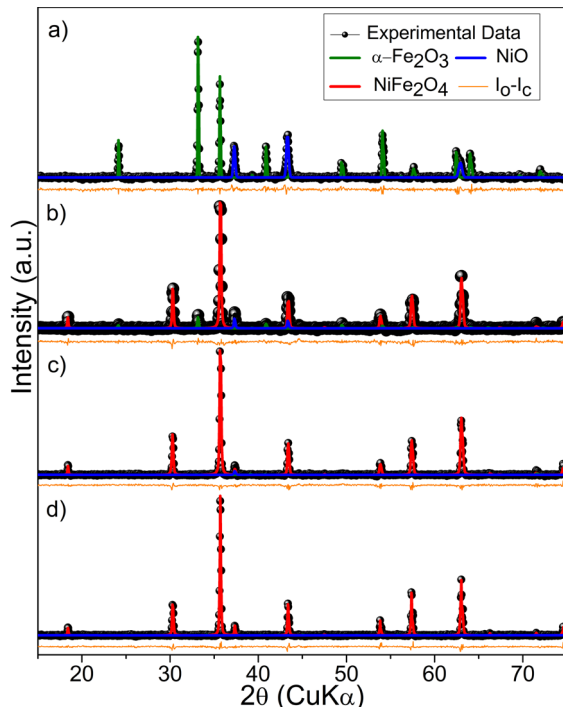

Figure 2. Rietveld analysis of the XRD patterns of (a) the initial mixture of reactants and of the samples submitted to heat treatments at (b) 1000 ºC, (c) 1100 ºC and (d) 1200 ºC. I$_o$-I$_c$ is the residue of the Rietveld refinement.

Figure 2(b) shows the Rietveld analysis of the XRD pattern of the sample submitted to heat treatment at 1000 °C. The XRD pattern was adjusted by introducing NiO (1010093 COD), α-Fe$_2$O$_3$ (9000139 COD) and NiFe$_2$O$_4$ (76179 ICSD) phases. The results showed that the abundances for NiO, α-Fe$_2$O$_3$ and NiFe$_2$O$_4$ are of 6 wt. %, 13 wt.% and 81 wt.%, respectively. The results indicate that this sample consists of a mixture of reactants and product, where the spinel phase has the largest abundance.

Figure 2(c) shows the Rietveld analysis of the XRD pattern of the sample submitted to heat treatment at 1100 °C. Most of the diffraction peaks were related to NiFe$_2$O$_4$; however, it is possible that small contributions from NiO and α-Fe$_2$O$_3$ be presented. The Rietveld analysis indicates that NiFe$_2$O$_4$ represents around 97 wt.% of the abundance in the sample. Figure 2(d) shows the Rietveld analysis of the XRD pattern of the sample submitted to heat treatment at 1200 °C.

Table 1. Variation with temperature of the relative abundances and of the lattice parameter of NiFe$_2$O$_4$. The conventional statistical parameters χ^2, R_{wp} and R_{exp} were obtained from the Rietveld analysis of the XRD patterns. Estimated errors are of about 1 wt. % for the phase abundances and of 0.001 Å for the lattice parameters.

Sample	NiO (wt.%)	α-Fe$_2$O$_3$ (wt.%)	NiFe$_2$O$_4$ (wt.%)	a (Å) (NiFe$_2$O$_4$)	R_{wp} (%)	R_{exp} (%)	χ^2
Initial mixture	32	68	---	---	9.23	7.65	1.46
1000 °C	6	13	81	8.333	8.46	7.11	1.42
1100 °C	< 1*	< 2*	97	8.336	7.27	6.35	1.31
1200 °C	---	---	100	8.340	7.65	6.58	1.35

*Values below or near to the XRD detection limit.

The XRD pattern was adjusted by introducing NiO (1010093 COD), α-Fe_2O_3 (9000139 COD) and $NiFe_2O_4$ (76179 ICSD). However, all diffraction peaks were related only to $NiFe_2O_4$ and no contributions coming from the reactants were detected. The lattice parameter obtained for $NiFe_2O_4$ was $a = 8.340$ Å, which is in the range of values reported in the literature [9,16]. The main findings of the Rietveld analysis are summarized in Table 1.

At this point, it is worth comparing the experimental lattice parameters of $NiFe_2O_4$ reported in Table 1 with the theoretical lattice parameter predicted by the formula of Hill *et al.* [17]. This formula can be applied only when cation reordering phenomena in spinel structure is considered. If we combine the equation of Hill *et al.*, with the equations of the average radius for the tetrahedral and the octahedral sites proposed by Sickafus *et al.* [18], we found that the theoretical lattice parameter, a_{th}, for $NiFe_2O_4$ can be expressed as follows:

$$a_{th} = a_0 + m\,\lambda \qquad (1)$$

in which λ is the inversion parameter, and:

$$a_0 = \frac{8}{3\sqrt{3}}\left[r_{Ni_A^{2+}} + (\sqrt{3})r_{Fe_B^{3+}} + (1+\sqrt{3})R_0\right] = 8.371 \text{ Å} \qquad (2)$$

$$m = \frac{8}{3\sqrt{3}}\left[-r_{Ni_A^{2+}} + \left(\frac{\sqrt{3}}{2}\right)r_{Ni_B^{2+}} + r_{Fe_A^{3+}} - \left(\frac{\sqrt{3}}{2}\right)r_{Fe_B^{3+}}\right] = -0.032 \text{ Å} \qquad (3)$$

where $r_{Ni_A^{2+}} = 0.55$ Å and $r_{Ni_B^{2+}} = 0.69$ Å are the ionic radii of the Ni^{2+} cations at tetrahedral (A) and octahedral [B] sites, respectively; $r_{Fe_B^{3+}} = 0.65$ Å and are the ionic radii (high spin) of the Fe^{3+} cations at (A) and [B] sites, respectively; and $R_0 = 1.38$ Å is the ionic radius of the O^{2-} anions. The range of values for the inversion parameter is $0 \le \lambda \le 1$.

It is worth mentioning that the numerical values of the a_0 and m constants are of vital importance to determine the range of values of the theoretical lattice parameter, a_{th}, in $NiFe_2O_4$. Equations (2) and (3) explicitly show the dependence of these constants with the ionic radii, oxidation states and coordination sites of the different ions in the spinel structure. From equation (1), it is observed that a_{th} decreases linearly as λ increases. The theoretical lattice parameter reaches maximum and minimum values of 8.371 Å (λ = 0) and 8.339 Å (λ = 1), respectively. On the other hand, it is expected that as the temperature increases, λ tends to 1 in $NiFe_2O_4$, which represents the more thermodynamically stable and the inversely ordered phase. Notice that the experimental lattice parameters for the samples with heat treatments at 1000 °C and 1100 °C are out of the range of a_{th} values, and are below $a_{th,min}$. Moreover, the experimental lattice parameters increase as temperature increase, contrary to what is expected if equation (1) is used, and if λ increase with temperature increase.

Therefore, the changes in the experimental lattice parameters with temperature cannot be ascribed to only cation reordering phenomena. A possible explanation is the presence of defects, like O, Ni and Fe vacancies that are gradually filled with ions as the temperature of the heat treatment increases.

Figure 3(a) shows the Mössbauer spectrum of the initial mixture of reactants. The spectrum was adjusted by introducing a single sextet assigned to Fe^{3+} ions in α-Fe_2O_3. The hyperfine parameters obtained from the fit were δ=0.36 mm/s, 2ε=-0.11 mm/s and B=51.4 T. All previous parameters are in agreement with the hyperfine parameters reported in the literature for α-Fe_2O_3 with micrometric particle size [19].

Figure 3(b) shows the Mössbauer spectrum of the sample with heat treatment at 1000 °C. The spectrum was adjusted by introducing three sextet components related to the α-Fe_2O_3 and $NiFe_2O_4$ phases. The first component corresponds to the sextet used to fit the Mössbauer spectrum of the initial mixture of reactants. This sextet has a spectral area of 28.0 % and was related to α-Fe_2O_3. The other two sextets were assigned to Fe^{3+} ions that occupy (A) and [B] sites in $NiFe_2O_4$. The hyperfine parameters (listed in Table 2) are in good agreement with those reported in the literature for $NiFe_2O_4$ [20-21].
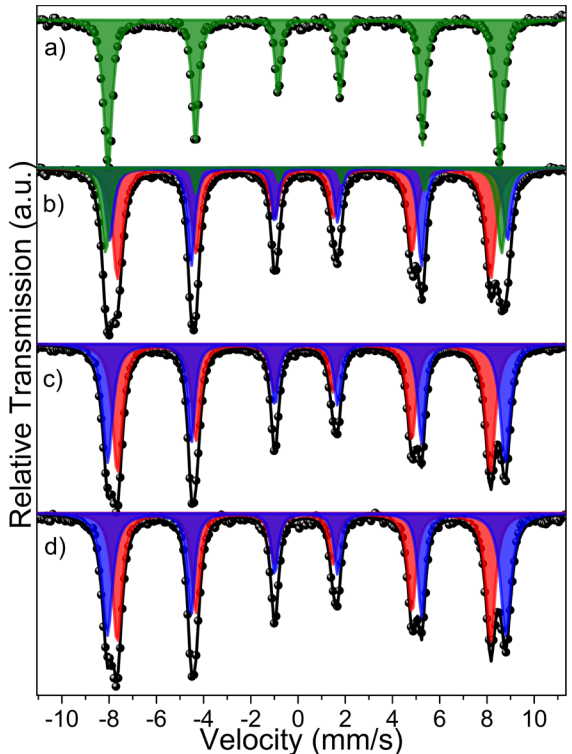

Figure 3. Mössbauer spectra of (a) the initial mixture of reactants and of the samples submitted to heat treatments at (b) 1000 ºC, (c) 1100 ºC and (d) 1200 ºC. The green sextet was related to α-Fe_2O_3, whereas the red and blue sextets were related to the (A) and [B] sites of $NiFe_2O_4$, respectively.

Cation Vacancies in NiFe$_2$O$_4$ During Heat Treatments at High Temperatures: Structural, Morphological and Magnetic Characterization

5

Table 2. Hyperfine parameters for the (A) and [B] sites of NiFe$_2$O$_4$. δ_A and δ_B are the isomer shifts, $2\varepsilon_A$ and $2\varepsilon_B$ are the quadrupole shifts, B_A and B_B are the hyperfine magnetic fields, and A_A and A_B are the relative spectral areas for irons at (A) and [B] sites, respectively.

Sample	δ_A (mm/s)	$2\varepsilon_A$ (mm/s)	B_A (T)	A_A (%)	δ_B (mm/s)	$2\varepsilon_B$ (mm/s)	B_B (T)	A_B (%)	A_A/A_B
1000 ºC	0.25	0	49	45	0.36	0	52.3	27	1.67
1100 ºC	0.25	0	49	52	0.36	0	52.3	48	1.08
1200 ºC	0.25	0	49	50	0.36	0	52.3	50	1

Figures 3(c-d) show the Mössbauer spectra of the samples submitted to heat treatments at 1100 °C and 1200 °C, respectively. The spectra were adjusted by introducing the two sextets of NiFe$_2$O$_4$ similarly as the fitting of the Mössbauer spectrum for the sample with heat treatment at 1000 °C. The hyperfine parameters are reported in Table 2. The Mössbauer spectrum of the sample with heat treatment at 1100 °C did not show the presence of α-Fe$_2$O$_3$, in agreement with the XRD pattern of this sample, for which there are no evident diffraction peaks related to α-Fe$_2$O$_3$.

However, the subspectral areas ratio for Fe^{3+} cations at tetrahedral (A) and octahedral [B] sites, A_A/A_B, decreases as the temperature increases. To understand the variation of this area ratio with temperature, it is worth recalling the typical formula of A_A/A_B used in Mössbauer spectrometry for materials with spinel structure [22-23]:

$$\frac{A_A}{A_B} = \left(\frac{f_A}{f_B}\right)\left(\frac{\lambda}{2-\lambda}\right) \qquad (4)$$

where $\frac{f_A}{f_B}$ is the recoilless f-factors ratio for Fe^{3+} cations at (A) and [B] sites. Using equation (4) and considering $\frac{f_B}{f_A}$ at room temperature (RT) [24]; we found $\frac{A_A}{A_B} = 0$ for $\lambda = 0$, and $\frac{A_A}{A_B} = 0.92$ for $\lambda = 1$. Notice that the experimental values of $\frac{A_A}{A_B}$ reported in Table 2 are outside the range of expected theoretical values. Of course, equation (4) can only be used when cation disordering is present in NiFe$_2$O$_4$. Taking into account that the Mössbauer subspectral areas are proportional to the number of Fe ions, the observed decrease in A_A/A_B with increasing temperature can be explained if it is assumed that there are Fe^{3+} vacancies mainly at the [B] sites, and that these are gradually filled with cations as the temperature of the heat treatment increases. Another interesting observation is that Mössbauer spectrometry could not detect the presence of Fe^{2+} ions in none of the samples, therefore oxygen vacancies, V_O, can be ruled out. In fact, V_O is likely accompanied with Fe^{2+} ions [25].

Finally, Mössbauer spectroscopy is a highly sensitive technique that allows to determine the oxidation states of the Fe atoms in matter. In the Mossbauer spectra of the samples, we obtained isomer shift values of 0.25 mm/s (relative to α-Fe) for Fe cations at tetrahedral sites, and of 0.36 mm/s (relative to α-Fe) for Fe cations at octahedral sites, which clearly point out to the presence of Fe^{3+} cations. In fact, if Fe^{2+} cations were presented, then higher isomer shift values (higher values than about 0.6 mm/s) should be expected.

These results clearly indicate that Fe^{2+} cations were not detected in the samples.

Figure 4 shows the IR spectra of the initial mixture of reactants and of the samples submitted to heat treatments. The IR spectrum of the sample without heat treatment (Fig. 4(a)) exhibits two absorption bands at 472 and 540 cm^{-1}. For the NiO phase, a main absorption band assigned to vibrations of the Ni-O bonds has been reported in the range 440-482 cm^{-1}[26-27]. The α-Fe$_2$O$_3$ phase has a characteristic absorption band in the range 460-480 cm^{-1} assigned to vibrations of the Fe-O bonds [28-29]. Therefore, the IR band located at 472 cm^{-1} is the result of the superposition of the absorption bands of NiO and α-Fe$_2$O$_3$. Finally, the absorption band at 540 cm^{-1} was assigned to vibrations of the Fe-O bonds in α-Fe$_2$O$_3$. This absorption band is characteristic of α-Fe$_2$O$_3$ and has been reported in the range 536-570 cm^{-1} [28-30].

Figures 4(b-d) show the IR spectra of the samples submitted to heat treatments. In general, it is observed that as the temperature increases, the absorption bands related to α-Fe$_2$O$_3$ and NiO disappear, and two new absorption bands at 411 and 599 cm^{-1} appear, which were related to NiFe$_2$O$_4$.
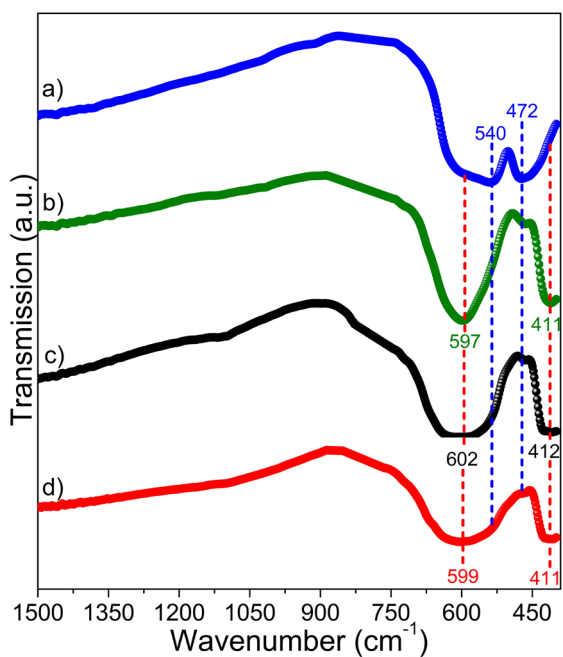
Figure 4. IR spectra of (a) the initial mixture of reactants and of the samples submitted to heat treatments at (b) 1000 ºC, (c) 1100 ºC and (d) 1200 ºC. The positions of the IR bands related to α-Fe$_2$O$_3$, NiO and NiFe$_2$O$_4$ are indicated in the spectra.

The absorption band at 411 cm^{-1} was assigned to vibrations of the Fe-O and Ni-O bonds in [B] sites of NiFe$_2$O$_4$ [31-32]. The absorption band at 599 cm^{-1} was assigned to vibrations of the Fe-O bonds in (A) sites of NiFe$_2$O$_4$ [31-32].

In the crystal structure of NiFe$_2$O$_4$, the Fe-O bonds vibrate with different frequencies (energy) depending on the coordination of iron. For example, to the vibrations of the Fe-O bonds at octahedral and tetrahedral sites are assigned IR bands at 411 cm^{-1} and 599 cm^{-1}, respectively. The different energy values in these vibrations are the result of the different distances between the Fe and O atoms in the spinel structure. In this case, the length of the Fe-O bond in (A) sites (0.189-0.191 nm) is less than the length of the Fe-O bond in [B] sites (0.203-0.205 nm) [16]. In Figure 4, it is noticed that as the temperature increases, the intensity of the IR band at 411 cm^{-1} increases in comparison to the intensity of the IR band at 599 cm^{-1}. If the intensities are related to the number of Fe-O bonds, then the observed variation in the relative intensities of these two IR bands can be explained if there are cation vacancies, mainly at the [B] sites, that are gradually filled with Fe^{3+} and Ni^{2+} cations as temperature of the heat treatment increases. This result is in good agreement with X-ray diffraction and Mössbauer spectroscopy.

Figure 5 shows the Raman spectra of the initial mixture of reactants and of the samples submitted to heat treatments. The spectrum of the sample without heat treatment (Fig. 5(a)) shows 6 Raman modes at 225, 244, 290, 410, 495 and 610 cm^{-1}, which were related to the Raman modes that the group theory predicts for α-Fe$_2$O$_3$ in the wavenumber range 100-1000 cm^{-1} [33-34]. On the other hand, for NiO the Raman bands are located at 570, 730 and 906 cm^{-1} [35-36], however, the bands for this material have very low intensities with respect to the bands of α-Fe$_2$O$_3$. In the Raman spectra, it was not possible to detect contributions from NiO even when zooming in the areas of interest.

Figures 5(b-d) show the Raman spectra of the samples submitted to heat treatments. In general, as the temperature increases, the Raman modes related to the reactants disappear in the spectra and 5 new Raman modes (A$_{1g}$ + 3F$_{2g}$ + E$_g$) related to NiFe$_2$O$_4$ appear [37-39]. The results obtained by Raman and IR spectroscopies confirm the synthesis of NiFe$_2$O$_4$.

Figure 6(a) shows that the initial mixture of reactants consists of agglomerates of micrometric particles. In our case, the reactants used in the synthesis of NiFe$_2$O$_4$ were α-Fe$_2$O$_3$ with particle size of about 4 μm and NiO with particle size smaller than 10 μm. However, the initial mixture of reactants was submitted to mechanical milling and for that reason, they exhibit particle sizes lower than 1 μm. Figures 6(b-d) show the SEM micrographs of the samples submitted to heat treatments at 1000, 1100 and 1200 °C, respectively. In general, it is observed that the samples consist of agglomerates of particles with irregular shapes and micrometric sizes. However, the average particle sizes seem to decrease as the temperature of heat treatment increases.
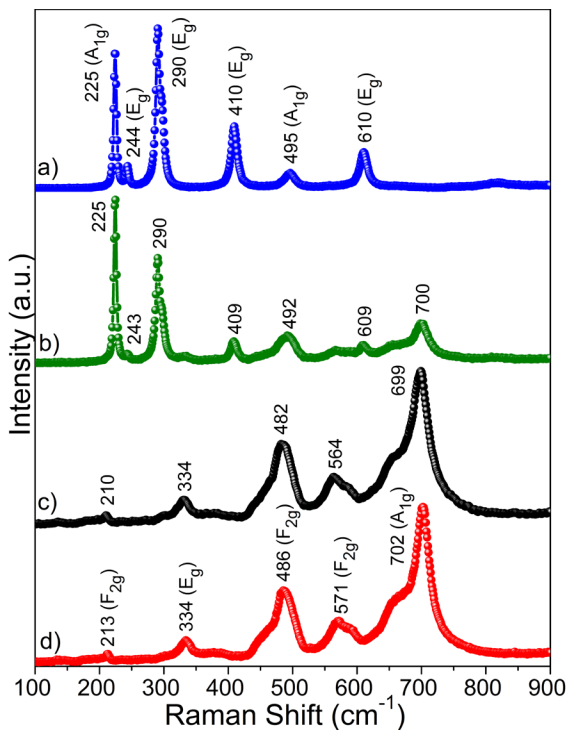

Figure 5. Raman spectra of (a) the initial mixture of reactants and of the samples submitted to heat treatments at (b) 1000 °C, (c) 1100 °C and (d) 1200 °C. The positions of the Raman bands and the corresponding symmetric representations were indicated in the spectra.
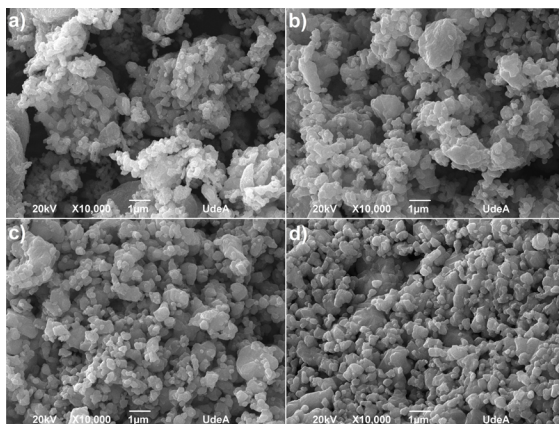

Figure 6. SEM micrographs of (a) the initial mixture of reactants and of the samples submitted to heat treatments at (b) 1000 °C, (c) 1100 °C and (d) 1200 °C.

Taking into account the previous SEM micrographs it is possible to infer that the sample with heat treatment at 1200 °C presents agglomerates of smaller particle sizes with respect to the samples treated at lower temperatures.

The elemental chemical composition of the samples was evaluated in three randomly assigned zones with no specific order. Figure 7 shows randomly selected zones in the SEM micrograph of the initial mixture of reactants, the idea is to obtain the percentages by weight of the chemical elements present in the evaluated area.
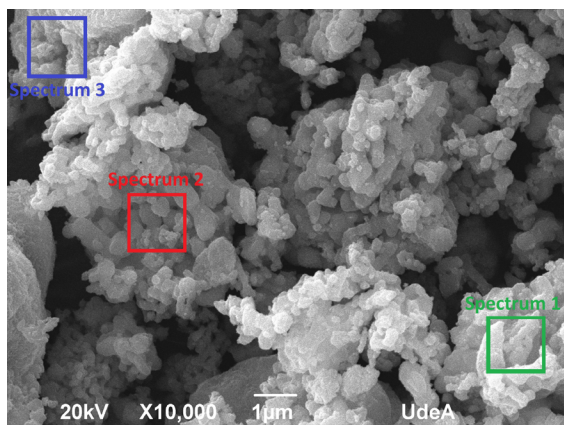
Cation Vacancies in NiFe$_2$O$_4$ During Heat Treatments at High Temperatures: Structural, Morphological and Magnetic Characterization

7

Figure 7. Selected zones in the SEM micrograph of the initial mixture of reactants for evaluation of elemental chemical composition.

This methodology allows to determine if the sample has homogeneous chemical composition, that is, if the percentages by weight of the chemical elements do not depend on the selected zone in the SEM micrograph. The previous procedure was also used in the samples with heat treatments at 1000, 1100 and 1200 °C.

Figure 8 shows the EDS spectra of the initial mixture of reactants and of the samples submitted to heat treatments. The spectra were obtained in the energy range 0-20 keV, however, to optimize the analysis and the identification of the chemical elements, the spectra were plotted in the 0.0-1.1 keV and 5.8-8.5 keV energy intervals, because in these ranges are located the contributions of the chemical elements detected in the samples.

In the EDS spectra of the initial mixture of reactants (Fig. 8(a)) is observed the presence of O, Fe and Ni. It is evident that the elemental chemical composition in this sample is not homogeneous because the EDS spectra depend on the evaluated zone in the SEM micrograph. In our case, the EDS spectra of the zones 1 and 2 (spectrum 1 and 2) indicate deficiencies and excesses in the amounts of Ni and Fe, respectively, while the EDS spectrum of the zone 3 (spectrum 3) represents the opposite case, that is, deficiencies and excesses in the amounts of Fe and Ni, respectively. The above indicates that the elemental chemical composition in this sample depends on the amount of NiO and/or α-Fe$_2$O$_3$ present in the evaluated zone. Figures 8(b-d) show the EDS spectra of the samples submitted to heat treatments at 1000, 1100 and 1200 °C. Initially, in the sample without heat treatment, the EDS spectra depended on the evaluated zone because each of them could contain more α-Fe$_2$O$_3$ or NiO. However, as the temperature of the heat treatment increases, the reactants interact chemically causing the formation of NiFe$_2$O$_4$ and the EDS spectra begin to coincide in the different evaluated zones in the SEM micrograph. In this way, the elemental chemical composition in the samples tends to be homogenous as the temperature of the heat treatment increases, which results in the formation of NiFe$_2$O$_4$ in the entire volume of the samples.
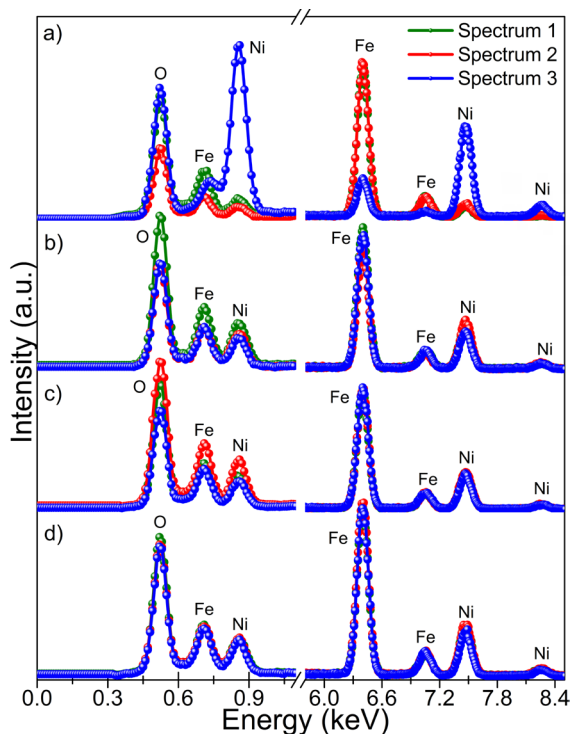

Figure 8. EDS spectra of (a) the initial mixture of reactants and of the samples submitted to heat treatments at (b) 1000 ºC, (c) 1100 ºC and (d) 1200 ºC. For each sample, the three spectral components are related to the randomly selected zones in the SEM micrograph.

The EDS spectra of the three zones for the sample with heat treatment at 1200 °C (Fig. 8(d)) are very similar and overlap over the entire range of energy, the above indicates that this sample is highly homogeneous in elemental chemical composition.

In summary, the EDS spectra were used only for qualitative analysis of chemical composition in order to show that: (i) there are no contaminants, (ii) the chemical elements Ni, Fe and O are presented in all samples, and (iii) the chemical composition becomes more homogeneous as the temperature of heat treatments increases.

Figure 9 shows the hysteresis loops of the initial mixture of reactants and of the samples submitted to heat treatments. The magnetization curves were obtained in the magnetic field interval [-1.0,+1.0] T at 300 K. The magnetization curve of the sample without heat treatment (Fig. 9(a)) represents the superposition of the magnetic behaviors of α-Fe$_2$O$_3$ and NiO. α-Fe$_2$O$_3$ exhibits weak ferromagnetism with saturation magnetization and coercive magnetic field of the order of 0.24 emu/g and 0.19 T, respectively [40]. On the other hand, NiO exhibits antiferromagnetism with saturation magnetization and coercive magnetic field of the order of 0.92×10^{-2} emu/g and 0.14×10^{-1} T, respectively [41-42]. The saturation magnetization and coercive magnetic field values of α-Fe$_2$O$_3$ are larger in several orders of magnitude to the obtained values for NiO, that is, α-Fe$_2$O$_3$ in the initial mixture of the reactants present the greatest contribution to the total magnetization of the sample.
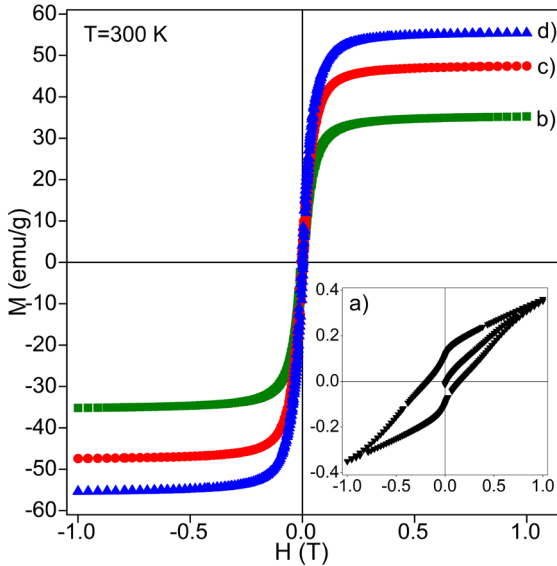
Figure 9. Hysteresis loops of (a) the initial mixture of reactants and of the samples submitted to heat treatments at (b) 1000 ºC, (c) 1100 ºC and (d) 1200 ºC.

The magnetization in the sample without heat treatment reaches a value of 0.36 emu/g, however, it was not possible to obtain its maximum value (saturation magnetization) even in the maximum value of the magnetic applied field (1.0 T). The coercive magnetic field has a value of 0.16 T, which indicates that the sample without heat treatment presents characteristics of hard magnetic materials (high coercive fields) and weak ferromagnetism at room temperature.

Figures 9(b-d) show the hysteresis loops of the samples submitted to heat treatments. In comparison to the initial mixture of reactants, drastic changes in the magnetic behavior of the samples were observed. The constant chemical interaction between the reactants results in the formation of NiFe$_2$O$_4$ characterized by having ferrimagnetic behavior at room temperature. The saturation magnetization, the coercive magnetic field, and the remanent magnetization values obtained in the analysis of the magnetization curves are reported in Table 3. The results indicate that as the temperature of the heat treatment increases, the saturation magnetization and the remanent magnetization increase, while the coercive magnetic field decreases.

Table 3. Saturation magnetization (M$_S$), remanent magnetization (M$_R$) and coercive magnetic field (H$_C$) values obtained in the analysis of the hysteresis loops.

Sample	M$_S$ (emu/g)	M$_R$ (emu/g)	H$_C$ (10^{-3} T)
Initial mixture	0.4	0.1	160
1000 ºC	35.2	4.0	5.0
1100 ºC	47.4	4.0	4.6
1200 ºC	55.4	4.4	3.2

With respect to the initial mixture of reactants, the saturation magnetization increases approximately 99.3% until reaching a maximum value of 55.4 emu/g, while the coercive magnetic field decreases by 99.3% until reaching a minimum value of 3.19×10^{-3} T in the sample with heat treatment at 1200 ºC. The heat treatments change the geometrical form of the hysteresis loops until adopting the S-type shape characteristic of the materials with ferrimagnetic behavior. From the results obtained in the hysteresis loops, it is possible to confirm the synthesis of NiFe$_2$O$_4$. As the temperature increases, hysteresis loops with S-type geometric form are obtained. This curve is characteristic of NiFe$_2$O$_4$ and represents its ferrimagnetic behavior at room temperature. The coercive field values indicate that the samples with heat treatments present characteristics of soft magnetic materials (low coercive fields) like NiFe$_2$O$_4$ [43]. The saturation magnetization (55.40 emu/g) is in good agreement with the values reported in the literature for NiFe$_2$O$_4$ [2,15].

It is important to analyze in more detail the results obtained for the saturation magnetization (M$_S$) in the samples with heat treatments, and to compare them with the theoretical saturation magnetization. In the unit cell of NiFe$_2$O$_4$, the Ni^{2+} cations occupy [B] sites, whereas the Fe^{3+} cations occupy (A) and [B] sites simultaneously. The Fe^{3+} and Ni^{2+} cations have magnetic moments of 5μ$_B$ and 2μ$_B$, respectively, where μ$_B$ is the Bohr magneton. The magnetization in NiFe$_2$O$_4$ is originated from the magnetic moments of the Ni^{2+} cations at [B] sites. The contribution from the magnetic moments of the Fe^{3+} cations at (A) and [B] sites cancel each other, because they have opposite orientations[44]. To perform a quantitative analysis, we consider the structural formula for NiFe$_2$O$_4$, which is given by:

$$(Ni^{2+}_{1-\lambda}Fe^{3+}_{\lambda})_A [Ni^{2+}_{\lambda}Fe^{3+}_{2-\lambda}]_B O^{2-}_4 \qquad (5)$$
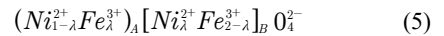
where () and [ ] represent the cations at tetrahedral (A) and octahedral [B] sites, respectively, and the parameter λ is the degree of inversion.

Per formula unit, the theoretical saturation magnetization, M_{the}, for an ideal collinear ferrimagnet, which is the case of NiFe$_2$O$_4$, is given by:

$$M_{the} = M_B - M_A \qquad (6)$$

where M_A and M_B are the magnetizations (per formula unit) of the sublattices (A) and [B] respectively, and are given by:

$$M_A = (1 - \lambda)M_{Ni^{2+}} + \lambda M_{Fe^{3+}} \qquad (7)$$

$$M_B = \lambda M_{Ni^{2+}} + (2 - \lambda)M_{Fe^{3+}} \qquad (8)$$

where M$_{Ni^{2+}}$ and M$_{Fe^{3+}}$ are the magnetic moments of the Ni^{2+} ($3d^8$, M$_{Ni^{2+}} = 2$μ$_B$) and Fe^{3+} ($3d^5$, M$_{Fe^{3+}} = 5$μ$_B$) cations, respectively. By replacing equations (7) and (8) into equation (6), we obtain:

$$M_{the} = 2(4 - 3\lambda)\mu_B \qquad (9)$$

Cation Vacancies in NiFe$_2$O$_4$ During Heat Treatments at High Temperatures: Structural, Morphological and Magnetic Characterization

9

From equation (9), it is noticed that as λ increases from 0 to 1, M_{the} decreases. On the other hand, it is expected that as the temperature increases, λ also increases, because the thermodynamic equilibrium state is gradually reached in NiFe$_2$O$_4$. Therefore, it would be expected that as the temperature increases, M_S decreases. However, in contrast, we found experimentally that M$_S$ increases as the temperature increases. This result implies that cation reordering phenomena cannot be considered as the dominant explanation for the obtained results, which is in agreement with all the results previously discussed.

4. Discussion

We have found that as the temperature of the heat treatments increases from 1000 °C to 1200°C, the NiFe$_2$O$_4$ production increases from 81 to 100 wt.%. The XRD analysis and the magnetization measurements of NiFe$_2$O$_4$ showed that as the temperature increases, there is an increase in the lattice parameter and in the saturation magnetization, but there is a decrease in the coercivity. On the other hand, Mössbauer spectroscopy showed that there is a decrease in the subspectral areas ratio for Fe^{3+} cations at (A) and [B] sites, A$_A$/A$_B$, with increasing temperature. From IR spectra, the intensity of the 411 cm^{-1} band (vibrations at octahedral sites) increases relative to the intensity of the 599 cm^{-1} band (vibrations at tetrahedral sites) with increasing temperature. These results suggest that a defective spinel NiFe$_2$O$_4$ is formed at 1000 °C, and that as the temperature increases, the defects gradually disappear. There are at least three possible hypotheses to explain the observed results: evaporation of chemical elements, cation reordering in the spinel structure and [B] sites cation vacancy filling. Let us discuss each of them. In the solid-state reaction processes, high temperatures are required because at room temperature solid materials do not react each other even if the conditions for thermodynamic reaction are favorable. There is no general method that indicates which is the ideal temperature to achieve the synthesis of a particular material, however, to activate diffusion processes in a mixture of reactants, it is required at least 2/3 of the melting temperature of the reactant with the lowest melting point. In most cases, the ideal temperature is determined by multiple assays using temperatures above the suggested temperature. In our case, the reactants used in the synthesis of NiFe$_2$O$_4$ correspond to nickel oxide (NiO) and hematite (α-Fe$_2$O$_3$) with melting points of 1955 °C and 1565 °C, respectively. The heat treatments were performed at temperatures generally higher than 1000 °C but lower than the melting points of the reactants involved in the synthesis. Therefore, the evaporation of chemical elements is not possible in the range of temperatures (1000-1200 °C) used in the synthesis. On the other hand, as carefully discussed in the Results section, cation reordering phenomena cannot be considered as the dominant explanation for the results.

The results can be nicely explained if it is assumed that [B]-sites cation vacancies are gradually filled with cations as the temperature of heat treatment increases. Therefore, we propose a general chemical formula for the defective nickel ferrite given by $(Ni^{2+}_{1-\lambda} Fe^{3+}_{\lambda})_A [Ni^{2+}_{\lambda-x} Fe^{3+}_{2-\lambda-y} V_{x+y}]_B O^{2-}_4$, where λ is the inversion parameter, and V stands for the Ni^{2+} and Fe^{3+} vacancies at [B] sites, with x and y concentrations, respectively. Of course, x and y tend to zero as the temperature increases. By using this chemical formula and assuming that the cation vacancies are non-magnetic and that the magnetic moments are collinear, then it is found that:

$$M_{the} = [2(4 - 3\lambda) - (2x + 5y)]\mu_B \qquad (10)$$

Notice that for a given λ, as x and y tend to cero, M_{the} increases, which is in accordance with the behavior of the saturation magnetization in the hysteresis loops. Possible spin canting and presence of magnetic defects could also contribute to change of the magnetic signal.

5. Conclusions

Nickel ferrite (NiFe$_2$O$_4$) was synthesized by mixing stoichiometric amounts of α-Fe$_2$O$_3$ and NiO using mechanical milling and heat treatments at high temperatures. The Rietveld analysis of the XRD patterns showed that the weight percentages of the reactants decreased with the increase of the temperature, while the weight percentage of NiFe$_2$O$_4$ had strict increasing behavior. The lattice parameter of NiFe$_2$O$_4$ was found to increase with increasing temperature. The Mössbauer spectra were fitted using three sextets related to the α-Fe$_2$O$_3$ and NiFe$_2$O$_4$ phases. As the temperature of the heat treatment increased, the sextet related to α-Fe$_2$O$_3$ disappeared and only the sextets related to Fe^{3+} cations (A) and [B] sites of NiFe$_2$O$_4$ remained. The infrared and Raman spectroscopies confirmed the formation of NiFe$_2$O$_4$. The IR spectra showed the characteristic absorption bands of NiFe$_2$O$_4$, which were related to metal-oxygen vibrations in tetrahedral and octahedral sites of the spinel structure, while the Raman spectra showed the characteristic active modes of this type of crystal structure. In the SEM micrographs it was observed that the samples consisted of particles with irregular shapes and micrometric sizes. The EDS spectra showed the presence of O, Fe and Ni ruling out the presence of impurities. The elementary chemical composition in the samples tended to be homogenous as the temperature of the heat treatment increases resulting in the formation of NiFe$_2$O$_4$. From the results obtained in the magnetization curves, it was possible to confirm the synthesis of NiFe$_2$O$_4$. As the temperature of the heat treatment increases, hysteresis loops with S-type geometric forms were obtained. This curve is characteristic of NiFe$_2$O$_4$ and represents its ferrimagnetic behavior. The saturation magnetization was in agreement with the values reported in literature for NiFe$_2$O$_4$.

All the results suggest that a defective spinel $NiFe_2O_4$ is formed at 1000 °C, and that as the temperature increases, the defects gradually disappear. Neither cation reordering phenomena nor possible evaporation of chemical elements were the dominant effects to account for the results. The results can be nicely explained if it is assumed that [B]-sites cation vacancies are gradually filled with cations as the temperature of the heat treatments increases.

6. Acknowledgments

7. References

1. Tangcharoen T, Ruangphanit A, Pecharapa W. Structural and magnetic properties of nanocrystalline zinc-doped metal ferrites (metal=Ni; Mn; Cu) prepared by sol-gel combustion method. *Ceramics International.* 2013;39(Suppl 1):S239-S243.

2. Šepelák V, Baabe D, Mienert D, Schultze D, Krumeich F, Litterst FJ, Becker KD. Evolution of structure and magnetic properties with annealing temperature in nanoscale high-energy-milled nickel ferrite. *Journal of Magnetism and Magnetic Materials*. 2003;257(2-3):377-386.

3. Caffrey NM, Fritsch D, Archer T, Sanvito S, Ederer C. Spin-filtering efficiency of ferrimagnetic spinels $CoFe_2O_4$ and $NiFe_2O_4$. *Physical Review B*. 2013;87(2):024419.

4. Rana S, Gallo A, Srivastava RS, Misra RDK. On the suitability of nanocrystalline ferrites as a magnetic carrier for drug delivery: Functionalization, conjugation and drug release kinetics. *Acta Biomaterialia*. 2007;3(2):233-242.

5. Bakr AA, Moustafa YM, Motawea EA, Yehia MM, Khalil MMH. Removal of ferrous ions from their aqueous solutions onto $NiFe_2O_4$-alginate composite beads. *Journal of Environmental Chemical Engineering*. 2015;3(3):1486-1496.

6. George M, John AM, Nair SS, Joy PA, Anantharaman MR. Finite size effects on the structural and magnetic properties of sol-gel synthesized $NiFe_2O_4$ powders. *Journal of Magnetism and Magnetic Materials*. 2006;302(1):190-195.

7. Ahlawat A, Sathe VG, Reddy VR, Gupta A. Mossbauer, Raman and X-ray diffraction studies of superparamagnetic $NiFe_2O_4$ nanoparticles prepared by sol-gel auto-combustion method. *Journal of Magnetism and Magnetic Materials*. 2011;323(15):2049-2054.

8. Cvejić Ž, Đurđić E, Ivković Ivandekić G, Bajac B, Postolache P, Mitoseriu L, et al. The effect of annealing on microstructure and cation distribution of $NiFe_2O_4$. *Journal of Alloys and Compounds*. 2015;649:1231-1238.

9. Bid S, Sahu P, Pradhan SK. Microstructure characterization of mechanosynthesized nanocrystalline $NiFe_2O_4$ by Rietveld's analysis. *Physica E: Low-dimensional Systems and Nanostructures*. 2007;39(2):175-184.

10. Salazar-Tamayo H, Márquez MA, Barrero CA. Effect of machine variables in the mechanosynthesis of $NiFe_2O_4$: a microstructural and kinematical study. *Powder Technology*. 2016;289:126-134.

11. Prabhakaran T, Hemalatha J. Combustion synthesis and characterization of highly crystalline single phase nickel ferrite nanoparticles. *Journal of Alloys and Compounds*. 2011;509(25):7071-7077.

12. Anupama MK, Srinatha N, Matteppanavar S, Angadi B, Sahoo B, Rudraswamy B. Effect of Zn substitution on the structural and magnetic properties of nanocrystalline $NiFe_2O_4$ ferrites. *Ceramics International*. 2018;44(5):4946-4954.

13. Gunjakar JL, More AM, Shinde VR, Lokhande CD. Synthesis of nanocrystalline nickel ferrite ($NiFe_2O_4$) thin films using low temperature modified chemical method. *Journal of Alloys and Compounds*. 2008;465(1-2):468-473.

14. Ivanov VG, Abrashev MV, Iliev MN, Gospodinov MM, Meen J, Aroyo MI. Short-range *B*-site ordering in the inverse spinel ferrite $NiFe_2O_4$. *Physical Review B*. 2010;82(2):024104.

15. Ceylan A, Ozcan S, Ni C, Ismat S. Solid state reaction synthesis of $NiFe_2O_4$ nanoparticles. *Journal of Magnetism and Magnetic Materials*. 2008;320(6):857-863.

16. Rais A, Taibi K, Addou A, Zanoun A, Al-Douri Y. Copper substitution effect on the structural properties of nickel ferrites. *Ceramics International*. 2014;40(9 Pt A):14413-14419.

17. Hill RJ, Craig JR, Gibbs GV. Systematics of the spinel structure type. *Physics and Chemistry of Minerals*. 1979;4(4):317-339.

18. Sickafus KE, Wills JM, Grimes NW. Structure of spinel. *Journal of the American Ceramic Society*. 1999;82(12):3279-3292.

19. Sánchez LC, Arboleda JD, Saragovi C, Zysler RD, Barrero CA. Magnetic and structural properties of pure hematite submitted to mechanical milling in air and ethanol. *Physica B: Condensed Matter*. 2007;389(1):145-149.

20. Kim SJ, Kim WC, Kim CS, Lee SW. Mössbauer studies of superexchange interactions in $NiFe_2O_4$. *Journal of the Korean Physical Society*. 2000;36(6):430-434.

21. Jacob J, Abdul M. Investigation of mixed spinel structure of nanostructured nickel ferrite. *Journal of Applied Physics*. 2010;107(11):114310.

22. Šepelák V, Bergmann I, Feldhoff A, Heitjans P, Krumeich F, Menzel D, et al. Nanocrystalline nickel ferrite $NiFe_2O_4$: mechanosynthesis, nonequilibrium cation distribution, canted spin arrangement, and magnetic behavior. *The Journal of Physical Chemistry C*. 2007;111(13):5026-5033.

23. Šepelák V, Indris S, Heitjans P, Becker KD. Direct determination of the cation disorder in nanoscale spinels by NMR, XPS, and Mössbauer spectroscopy. *Journal of Alloys and Compounds*. 2007;434-435:776-778.

24. Salazar-Tamayo H, García KE, Barrero CA. New method to calculate Mössbauer recoilless *f*-factors in $NiFe_2O_4$. Magnetic, morphological and structural properties. *Journal of Magnetism and Magnetic Materials*. 2019;471:242-249.

25. Lüders U, Bibes M, Bobo JF, Cantoni M, Bertacco R, Fontcuberta J. Enhanced magnetic moment and conductive behavior in $NiFe_2O_4$ spinel ultrathin films. *Physical Review B*. 2005;71(13):134419.

Cation Vacancies in NiFe$_2$O$_4$ During Heat Treatments at High Temperatures: Structural, Morphological and Magnetic Characterization

11

26. Shibli SMA, Harikrishnan GJ, Anupama VR, Chinchu KS, Meena BN. Development of nano NiO incorporated nickel-phosphorus coatings for electrocatalytic applications. *Surface and Coatings Technology*. 2015;262:48-55.

27. Wang Y, Zhu J, Yang X, Lu L, Wang X. Preparation of NiO nanoparticles and their catalytic activity in the thermal decomposition of ammonium perchlorate. *Thermochimica Acta*. 2005;437(1-2):106-109.

28. Woo K, Lee HJ, Ahn JP, Park Y. Sol-Gel Mediated Synthesis of Fe$_2$O$_3$ Nanorods. *Advanced Materials*. 2003;15(20):1761-1764.

29. Nag S, Roychowdhury A, Das D, Mukherjee S. Synthesis of α-Fe$_2$O$_3$-functionalised graphene oxide nanocomposite by a facile low temperature method and study of its magnetic and hyperfine properties. *Materials Research Bulletin*. 2016;74:109-116.

30. Sahoo SK, Agarwal K, Singh AK, Polke BG, Raha KC. Characterization of γ- and α-Fe$_2$O$_3$ nano powders synthesized by emulsion precipitation-calcination route and rheological behaviour of α-Fe$_2$O$_3$. *International Journal of Engineering, Science and Technology*. 2010;2(8):118-126.

31. Jacob BP, Kumar A, Pant RP, Singh S, Mohammed EM. Influence of preparation method on structural and magnetic properties of nickel ferrite nanoparticles. *Bulletin of Materials Science*. 2011;34(7):1345-1350.

32. Sattar AA, El-Sayed HM, Alsuqia I. Structural and magnetic properties of CoFe$_2$O$_4$/NiFe$_2$O$_4$ core/shell nanocomposite prepared by the hydrothermal method. *Journal of Magnetism and Magnetic Materials*. 2015;395:89-96.

33. Legodi MA, de Waal D. The preparation of magnetite, goethite, hematite and maghemite of pigment quality from mill scale iron waste. *Dyes and Pigments*. 2007;74(1):161-168.

34. de Faria DLA, Lopes FN. Heated goethite and natural hematite: Can Raman spectroscopy be used to differentiate them? *Vibrational Spectroscopy*. 2007;45(2):117-121.

35. Thema F, Manikandan E, Gurib-Fakim A, Maaza M. Single phase Bunsenite NiO nanoparticles green synthesis by *Agathosma betulina* natural extract. *Journal of Alloys and Compounds*. 2016;657:655-661.

36. Mendoza L, Baddour-Hadjean R, Cassir M, Pereira-Ramos JP. Raman evidence of the formation of LT-LiCoO$_2$ thin layers on NiO in molten carbonate at 650°C. *Applied Surface Science*. 2004;225(1-4):356-361.

37. Lazarević ZŽ, Jovalekić Č, Rečnik A, Ivanovski VN, Milutinović A, Romčević M, et al. Preparation and characterization of spinel nickel ferrite obtained by the soft mechanochemically assisted synthesis. *Materials Research Bulletin*. 2013;48(2):404-415.

38. de Paiva JAC, Graça MPF, Monteiro J, Macedo MA, Valente MA. Spectroscopy studies of NiFe$_2$O$_4$ nanosized powders obtained using coconut water. *Journal of Alloys and Compounds*. 2009;485(1-2):637-641.

39. Chen T, Tang Q, Wang B, Li Y, Liu L. Dielectric and magnetic properties of poly (vinylidene fluoride) composites doped with pomegranate-like PPY@NiFe$_2$O$_4$ nanospheres. *Materials Letters*. 2015;159:413-416.

40. Sivakumar S, Anusuya D, Khatiwada CP, Sivasubramanian J, Venkatesan A, Soundhirarajan P. Characterizations of diverse mole of pure and Ni-doped α-Fe$_2$O$_3$ synthesized nanoparticles through chemical precipitation route. *Spectrochimica Acta Part A: Molecular and Biomolecular Spectroscopy*. 2014;128:69-75.

41. Sathishkumar K, Shanmugam N, Kannadasan N, Cholan S, Viruthagiri G. Infuence of Zn^{2+} ions incorporation on the magnetic and pseudo capacitance behaviors of NiO nanoparticles. *Materials Science in Semiconductor Processing*. 2014;27:846-853.

42. Salavati-Niasari M, Entesari M. Controlled synthesis of spherical α-Ni(OH)$_2$ hierarchical nanostructures via a simple hydrothermal process and their conversion to NiO. *Polyhedron*. 2012;33(1):302-309.

43. Hajalilou A, Hashim M, Ebrahimi-Kahrizsangi R, Mohamed kamari H, Sarami N. Synthesis and structural characterization of nano-sized nickel ferrite obtained by mechanochemical process. *Ceramics International*. 2014;40(4):5881-5887.

44. Marinca TF, Chicinaş I, Isnard O, Popescu V. Nanocrystalline/Nanosized Ni$_{1-γ}$Fe$_{2+γ}$O$_4$ Ferrite Obtained by Contamination with Fe During Milling of NiO-Fe$_2$O$_3$ Mixture. Structural and Magnetic Characterization. *Journal of the American Ceramic Society*. 2013;96(2):469-475.